Electro-mechanical efficiency of plasma synthetic jet actuator driven by capacitive discharge

Zong, Haohua; Kotsonis, Marios

DOI
10.1088/0022-3727/49/45/455201

Publication date
2016

Document Version
Accepted author manuscript

Published in
Journal of Physics D: Applied Physics

Citation (APA)
Zong, H., & Kotsonis, M. (2016). Electro-mechanical efficiency of plasma synthetic jet actuator driven by capacitive discharge. *Journal of Physics D: Applied Physics*, *49*(45), Article 455204. https://doi.org/10.1088/0022-3727/49/45/455201

Electro-mechanical efficiency of plasma synthetic jet actuator driven by capacitive discharge

Haohua Zong* and Marios Kotsonis

Faculty of Aerospace Engineering, Delft University of Technology, Delft 2629 HS, Netherlands

Abstract: A simplified model is established to estimate the jet exit density variation of a plasma synthetic jet actuator (PSJA) driven by capacitive arc discharge. This model, in conjunction with phase-locked planar Particle Imaging Velocimetry (PIV) measurements, enables the calculation of jet mechanical energy for different operating conditions. Discharge energy is directly calculated based on waveforms of applied voltage and discharge current. The ratio of jet mechanical energy to discharge energy provides the absolute electro-mechanical efficiency. Results indicate that PSJA is characterized by a rather low electro-mechanical efficiency in the order of 0.1%, while the maximum observed value under tested conditions is 0.22%. Electro-mechanical efficiency improves significantly with nondimensional energy deposition, and appears largely independent of jet exit diameter.

Plasma-based flow control actuators, capitalizing on inherently fast response and robust structure, have been intensively researched in the past 15 years. Efforts towards developing novel-concept powerful actuators and improving control authority of existing actuators have been extensive [1-2]. A popular concept is the plasma synthetic jet actuator (PSJA), which relies on pulsed arc/spark discharge to rapidly pressurize the air in a confined cavity. Due to the rapid thermalization and pressurization of the cavity air, PSJA can produce a 5 kHz pulsed jet with a peak jet velocity as high as 250 m/s [3]. This wide-bandwidth high-intensity feature enables energetic and effective flow control in the areas of shock wave boundary layer interaction, airfoil flow separation control, and flight control [4-6].

The very fast issuing jet ($O(\mu s)$), small cavity scales ($O(mm)$) and strong electromagnetic interference due to the repetitive high voltage pulses render the characterization of PSJA challenging [7-8]. Until this point, experimental data related to the expelled gas mass per discharge cycle, impulse per jet pulse, and especially the electro-mechanical efficiency are largely not available. Without the support of these important experimental data, further steps towards optimizing actuator parameters and improving jet effectiveness can be difficult. This letter proposes a simplified analytical model to calculate the absolute electro-mechanical efficiency of PSJA, based on experimental data. Influence of both jet exit diameter and nondimensional energy deposition is analyzed.

For the purpose of this study, a three-electrode PSJA is adopted and fed by a sequential discharge (trigger discharge-capacitive discharge) power supply. As shown in Fig. 1, the actuator is comprised of a metal cap and a ceramic cylindrical cavity (height: 15 mm, diameter: 12 mm, volume: 1696 mm^3). Centre of the jet exit is set as the origin of the coordinate system. Configuration of the power supply is described in detail in Zong & Kotsonis [9], thus not repeated here. Five cases are investigated, as listed in Table 1. U_0 and C represent capacitor voltage and capacitance, respectively. Cases 1 to 3 pertain to variations of discharge energy, while Cases 2, 4 and 5, involve the variation of jet exit diameter (denoted as D). With PSJA regarded as an energy conversion system, input energy and output energy correspond to arc discharge energy and jet mechanical energy, respectively. Waveforms of arc discharge, as shown in Fig. 2, are measured by a high-voltage probe (LeCroy, PPE20kV) and current monitor (Pearson, Model 325), and recorded by an oscilloscope (Tektronix, TDS 3054C). Details on the discharge circuit are available in Zong & Kotsonis [9]. With discharge current chosen as the state variable, the mathematical model of discharge circuit (RLC series circuit) can be simplified as a second-order differential equation [10]. Its typical solution in underdamped condition is a periodically oscillating waveform with declining amplitude as shown in Fig. 2.

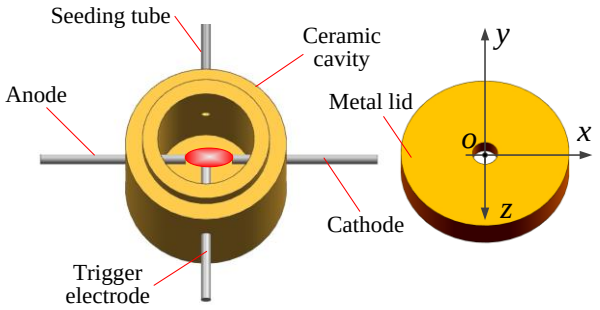

Fig. 1 Actuator structure: ceramic cavity (left) and metal lid (right). Red ellipse between the electrodes indicates the plasma region.

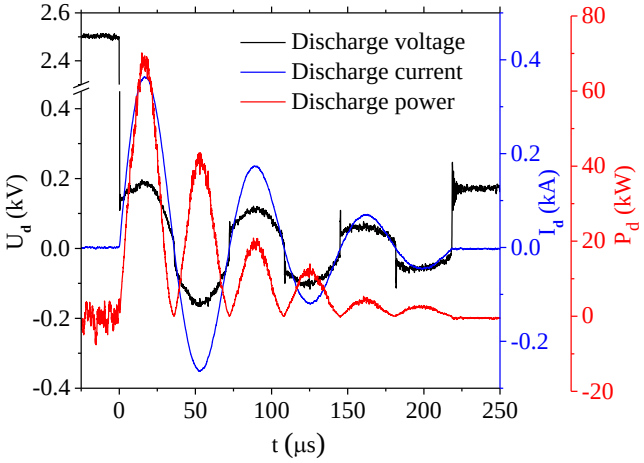

Fig. 2 Discharge waveforms for Case 3.

By integrating the product of discharge voltage (U_d) and discharge current (I_d), namely the instantaneous discharge power (P_d), arc discharge energy (E_d) for all cases are obtained. The ratio of discharge energy to internal energy of cavity gas (E_g) prior to discharge defines the nondimensional energy deposition (ε), as shown in Equation (1).

$$\varepsilon = \frac{E_d}{E_g} = \frac{\int_0^{T_d} U_d(t) I_d(t) dt}{C_v \rho_0 V_{ca} T_0} \quad (1)$$

*Email: H.zong-1@tudelft.nl

Where, C_v and V_{ca} are constant-volume specific heat capacity and the cavity volume, respectively. ρ_0 and T_0 denote ambient density and ambient temperature. T_d represents the discharge duration. For the investigated case (atmospheric condition, air medium), E_g is calculated to be 427 mJ. Discharge energy and nondimensional energy deposition are listed in Table.1.

Table 1 Actuator parameters and electrical parameters for all cases

	U_0 (kV)	C (μF)	D (mm)	E_d (mJ)	ε
Case 1	2.5	0.5	2	414	0.97
Case 2	2.5	1	2	1056	2.47
Case 3	2.5	2	2	2818	6.58
Case 4	2.5	1	1.5	1056	2.47
Case 5	2.5	1	3	1056	2.47

The mechanical energy of jet consists of two terms, namely the kinetic energy term and the pressure energy term, as shown in Equation (2).

$$E_m = \int_0^{T_{jet}} [\frac{p_e(t) - p_0}{\rho_e(t)} + 0.5 \cdot v_e^2(t)] \cdot \rho_e(t) v_e(t) A \cdot dt \qquad (2)$$

Where, $\rho_e(t)$, $v_e(t)$ and $p_e(t)$ are spatially-averaged exit density, exit velocity and exit pressure, respectively; p_0 is ambient pressure (1.007 bar). A denotes exit area, while T_{jet} represents total jet duration time.

Under the assumption of cylindrical symmetry, the jet exit velocity can be extracted from planar PIV results. In our experiments, a high resolution (16M pixels) camera and a separate seeding scheme in the actuator cavity are adopted, enabling a high spatial resolution of 12 vectors/mm in the core of the jet. The PIV system and the discharge system are synchronized, working in phase-locked mode. Recording rate of PIV system is 0.5 Hz. Time delay between the discharge initialization and PIV recording, namely the "phase", is denoted as t. For each phase, 200 images are recorded to ensure statistical convergence. A representative phase-averaged velocity field for Case 3 is shown in Fig. 3. A powerful high-speed jet and a distinctive front vortex ring are ensuing shortly after discharge ignition. By placing an interrogation window directly over the jet exit, change of spatially-averaged exit velocity can be monitored. A detailed description of the PIV setup and the used interrogation window can be found in Zong & Kotsonis [9].

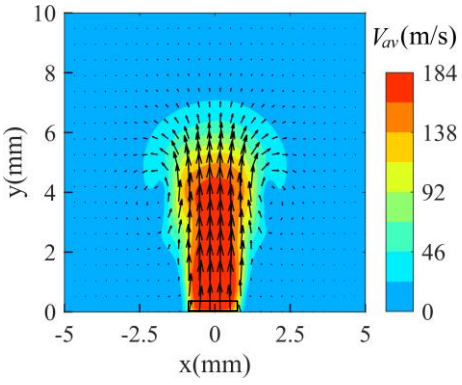

Fig. 3 Typical phase-averaged velocity field for Case 3. Elapsed time from ignition of discharge is t = 150 μs. Black rectangle above exit indicates the interrogation window. See Fig. 1 for the definition of coordinate system.

The variation of exit velocity is shown in Fig. 4 for all tested cases. Within one cycle of actuation, jet exit velocity initially increases sharply, then sustains a short period around the peak value, and finally diminishes slowly. A negative exit velocity (suction) indicates the termination of the jet stage, thus is used to determine jet duration time. Peak exit velocity ($U_{e,\max}$) and jet duration time (T_{jet}) are listed in Table 2 for all tested cases. As discharge energy increases (Cases 1-3), both peak exit velocity and jet duration time increase. Additionally, with constant discharge energy and increasing orifice diameter (Cases 2, 4 and 5), peak exit velocity is moderately affected, while jet duration time drops consistently.

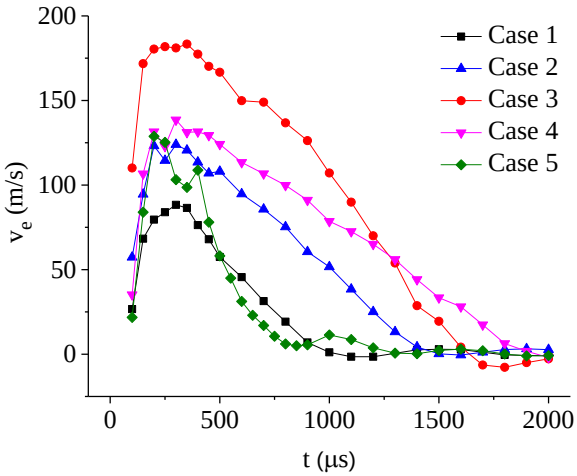

Fig. 4 Phase-averaged exit velocity in one period.

As exit velocity for all cases is subsonic, pressure term in Equation (2) can be neglected. A similar approach has been followed in Anderson and Knight [5]. The last obstacle in estimating jet mechanical energy is the unknown time-varying exit density. In order to estimate this, a simplified model for the jet stage is established here, as shown in Equation (3).

$$\begin{cases} d(\rho_{ca}(t) \cdot V_{ca}) / dt = -\rho_e(t) v_e(t) A \\ \rho_{ca}(t) / \rho_e(t) = [1 + \frac{\gamma - 1}{2} Ma_e^2(t)]^{1/(\gamma-1)} \\ Ma_e(t) = v_e(t) / \sqrt{\gamma R T_e(t)} \end{cases} \qquad (3)$$

$\rho_{ca}(t)$ denotes the time-varying spatially-averaged cavity density. $Ma_e(t)$ and $T_e(t)$ are jet exit Mach number and jet exit temperature. γ and R stand for gas specific heat ratio and gas constant, respectively. In Equation (3), the first formula is essentially the mass conservation law, while the second one is obtained under the assumption of isentropic expansion [5]. Apart from $v_e(t)$, totally four unknown variables (ρ_{ca} ρ_e , Ma_e and T_e) and three formulas are introduced. Obviously, Equation (3) is not closed and can't be directly solved.

The remainder of this paper turns to simplifying Equation (3), and estimating the lower limit and upper limit of time-varying exit density. The analytical solution of Equation (3) is derived as follows,

$$\begin{cases} \rho_{ca}(t) = \rho_0 / [f(t) \cdot \exp(\frac{A}{V_{ca}} \cdot \int_0^t \frac{v_e(t)}{f(t)} dt)] \\ f(t) = [1 + \frac{\gamma - 1}{2} Ma_e^2(t)]^{1/(\gamma-1)} \end{cases} \qquad (4)$$

Since the expelled gas is of high temperature, the relation $0 \le Ma_e(t) \le v_e(t) / \sqrt{\gamma R T_0}$ is always tenable. Thus, the upper

limit ($f_{UL}(t)$) and lower limit of function $f(t)$ are defined as $[1+(\gamma-1)\cdot v_e^{\,2}(t)/(2\gamma RT_0)]^{1/(\gamma-1)}$ and 1, respectively. Finally, the variation of exit density should lie in the following interval.

$$\begin{cases} \rho_{ca}(t) \geq \rho_0 / [\, f_{UL}(t) \cdot \exp(\dfrac{A}{V_{ca}} \cdot \int_0^t v_e(t)dt)] \\ \rho_{ca}(t) \leq \rho_0 / \exp(\dfrac{A}{V_{ca}} \cdot \int_0^t \dfrac{v_e(t)}{f_{UL}(t)}dt) \end{cases} \tag{5}$$

Based on Equation (5), the upper limit and the lower limit of exit density variation can be computed, as shown in Fig. 5.

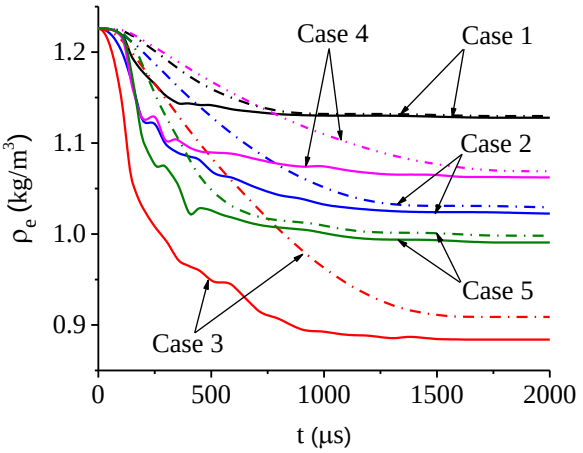

Fig. 5 Variation of exit density. The solid line and dash-dot line represent the lower limit and the upper limit, respectively.

Peak ratio of the upper limit to the lower limit for all cases is less than 1.16. Based on this, if the exit density is estimated by the mean value of two limits, the maximum relative error will be 8%. Using the calculated density, limits of the total expelled gas mass (m_e), jet impulse (I_p) and jet mechanical energy (E_m) can be calculated, based on Equation (6). It should be noted that the three integrated terms in Equation (6) are indeed the product of exit density and different orders of exit velocity.

$$\begin{cases} m_e = \int_0^{T_{jet}} \rho_e(t) v_e(t) A \cdot dt \\ I_p = \int_0^{T_{jet}} v_e(t) \cdot \rho_e(t) v_e(t) A \cdot dt \\ E_m = \int_0^{T_{jet}} 0.5 \cdot v_e^2(t) \cdot \rho_e(t) v_e(t) A \cdot dt \end{cases} \tag{6}$$

By choosing proper quantities, these three parameters can further be normalized, as shown in Equation (7).

$$\begin{cases} m_e^* = m_e / (\rho_0 V_{ca}) \\ I_p^* = I_p / \sqrt{2E_d \cdot (\rho_0 V_{ca})} \\ \eta_m = E_m / E_d \end{cases} \tag{7}$$

Where, $\rho_0 V_{ca}$ denotes the initial mass of cavity gas; η_m stands for the absolute electro-mechanical efficiency. The quantity $\sqrt{2E_d \cdot (\rho_0 V_{ca})}$ is derived under the assumption that the entire discharge energy E_d is transformed into kinetic energy of cavity gas (mass: $\rho_0 V_{ca}$, velocity: $\sqrt{2E_c / (\rho_0 V_{ca})}$). Obviously, the nondimensional impulse I_p^* has an upper limit of 1, and a meaning of "impulse efficiency". Limits of these performance parameters for all cases are listed in Table 2. As already mentioned, the true values of these parameters should lie in between two limits, but not necessarily at the middle.

As discharge energy increases, total expelled gas mass increases significantly from 8% to about 27%. When discharge energy remains unchanged, an increasing exit diameter results in a slightly rising expelled mass. This variation is attributed to the viscous drag on the actuator throat wall. In principle, viscous drag is linearly proportional to the perimeter of exit orifice, thus the orifice diameter. The instantaneous mass flow of the jet increases linearly with the exit area, namely the square of orifice diameter. Hence, the viscous drag imposed on unit mass flow is relatively larger for the case of small orifice diameter. This large viscous drag finally results in a small expelled gas mass.

As for nondimensional impulse and absolute electro-mechanical efficiency, mean values of their respective limits are plotted in Fig. 6 for all cases. Error bar directly corresponds to the maximum absolute error. It is striking that the absolute electro-mechanical efficiency of PSJA is quite low, in the order of 0.1%, very similar to that of the dielectric barrier discharge (DBD) plasma actuator [11]. As nondimensional energy deposition increases, electro-mechanical efficiency improves. Maximum value observed is 0.216% for all tested cases. This variation trend agrees well with that predicated by the thermodynamic cycle model in Zong et al. [12], where heating time and non-dimensional energy deposition are identified as the two major parameters affecting the thermodynamic cycle efficiency. In order to further improve the electro-mechanical efficiency of PSJA, either increasing discharge energy or decreasing cavity volume should be adopted. However, it should be noted that there exists a minimum cavity volume to physically accommodate the discharge electrodes. The nondimensional impulse is in the order of 1%. The trend of nondimensional impulse is almost identical to that of electro-mechanical efficiency as a function of nondimensional energy deposition. This verifies that nondimensional impulse can also be used to evaluate the electro-mechanical efficiency of PSJA.

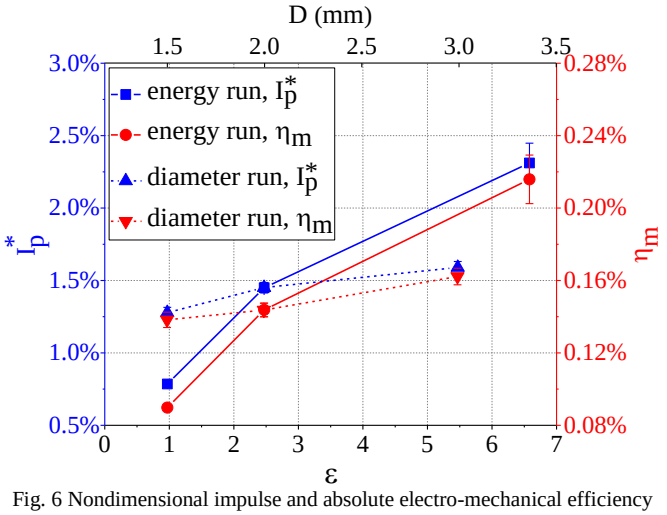

Fig. 6 Nondimensional impulse and absolute electro-mechanical efficiency

Compared with nondimensional energy deposition, the influence of orifice diameter is weak, although a slight improvement in nondimensional impulse and absolute electro-mechanical efficiency is observed with increasing orifice diameter. This agrees well with the results in Zong et al. [13]. Based on this observation, it is concluded that adjusting orifice diameter can only change the instantaneous issuing rate of jet mechanical energy and impulse, and will

not significantly alter the total amount of produced mechanical energy and impulse.

In conclusion, the absolute electro-mechanical efficiency of PSJA is in the order of 0.1%, and can be improved by increasing nondimensional energy deposition. This trend is quite different from that of discharge efficiency and heating efficiency of capacitive discharge, where increasing energy deposition will do harm to their improvement [10,14]. Orifice diameter can be used to tailor the instantaneous mass flow rate, and thus the jet duration time. However, it has little influence on peak exit velocity, nondimensional impulse, and electro-mechanical efficiency.

Table 2 Key performance parameters of PSJA

	$U_{e,\max}$ (m/s)	T_{jet} (μs)	m_e^*	I_p $(\mu N \cdot s)$	E_m (mJ)	I_p^*	η_m
Case 1	88	1000	7.66 %-7.82 %	10.2-10.4	0.367-0.377	0.776 %-0.795 %	0.0886 %-0.0910 %
Case 2	124	1400	15.9 %-16.5 %	29.6-31.1	1.48-1.56	1.42 %-1.49 %	0.140 %-0.148 %
Case 3	183	1600	25.4 %-28.3 %	74.5-83.8	5.71-6.46	2.18 %-2.45 %	0.202 %-0.229 %
Case 4	128	850	12.8 %-13.4 %	26.0-27.5	1.42-1.51	1.24 %-1.31 %	0.134 %-0.143 %
Case 5	138	1900	18.5 %-19.3 %	32.4-34.2	1.67-1.76	1.55 %-1.63 %	0.158 %-0.167 %

[1] L. N. Cattafesta, and M. Sheplak, Annu. Rev. Fluid Mech. 43, 247 (2011).

[2] T. C. Corke, C. L. Enloe, and S. P. Wilkinson, Annu. Rev. Fluid Mech. 42, 505 (2010).

[3] V. Narayanaswamy, L. Rajia, and N. T. Clemens, AIAA J. 48, 297 (2010).

[4] V. Narayanaswamy, L. Rajia, and N. T. Clemens, Phys. Fluids. 24, 076101 (2012).

[5] K. V. Anderson, and D. D. Knight, AIAA J. 50, 1855 (2012).

[6] T. Emerick, M. Y. Ali, C. Foster, F. S. Alvi, and S. Popkin, Exp. Fluids. 55, 1858 (2014).

[7] S. H. Popkin, B. Z. Cybyk, C. H. Foster, and F. S. Alvi, AIAA, J. 54, 1831 (2016).

[8] H. S. Ko, S. J. Haack, H. B. Land, B. Cybyk, J. Katz, and H. J. Kim, Flow Meas. Instrum. 21, 443 (2010).

[9] H. Zong and M. Kotsonis, J. Phys. D. 49, 335202 (2016).

[10] A. Belinger, N. Naude, J. P. Cambronne, and D. Caruana, J. Phys. D 47, 345202 (2014).

[11] R. H. M. Giepman and M. Kotsonis, Appl. Phys. Lett. 98, 221504 (2011).

[12] H. Zong , Y. Wu, H. Song, and M. Jia, AIAA J. (Published Online) DOI: 10.2514/1.J054987, (2016).

[13] H. Zong, Y. Wu, H. Song, H. Liang, Y. Li, and Z. Zhang, J. Phys. D 49, 025504 (2016).

[14] M. Golbabaei-Asl, D. Knight, and S. Wilkinson, AIAA J. 53, 501 (2015).